Luminescent transition metal dichalcogenide nanosheets through one-step liquid phase exfoliation

2D Materials

OPEN ACCESS

RECEIVED
10 March 2016

REVISED
29 July 2016

ACCEPTED FOR PUBLICATION
22 August 2016

PUBLISHED
1 September 2016

PAPER

Luminescent transition metal dichalcogenide nanosheets through one-step liquid phase exfoliation

M Mar Bernal[1], Lidia Álvarez[1], Emerson Giovanelli[1], Adriana Arnáiz[1], Luisa Ruiz-González[2], Santiago Casado[1], Daniel Granados[1], Ana M Pizarro[1], Andres Castellanos-Gomez[1] and Emilio M Pérez[1]

[1] IMDEA Nanociencia, Calle Faraday 9, Ciudad Universitaria de Cantoblanco, E-28049, Madrid, Spain
[2] Departamento de Química Inorgánica, Universidad Complutense de Madrid, Avenida Complutense s/n, E-28040, Madrid, Spain

E-mail: emilio.perez@imdea.org

Keywords: colloids, liquid phase exfoliation, photoluminescence, bioimaging, transition metal dichalcogenides

Supplementary material for this article is available online

Abstract

Liquid phase exfoliation (LPE) from the bulk is an adequate method for the mass-production of thin nanosheets of transition metal dichalcogenides (TMDCs). However, making suspensions in which the extraordinary properties of mechanically exfoliated TMDCs are observable remains a challenge. We describe a mild LPE method to produce luminescent suspensions of MoS_2 and WS_2 in *N*-methylpyrrolidone or isopropanol/water mixtures, without the need for a purification step. The key differences in our experimental procedure compared to previously reported LPE methods are the use of mild bath sonication at controlled temperature and the low initial concentration of the parent TMDC. Spectroscopic and AFM data confirm that an overwhelming majority of the sample is composed of ultrathin nanosheets. HREM data support the formation of the luminescent 2H polytype. The ultrathin nanosheets can be transferred to pure water and cell culture medium. Confocal fluorescence microscopy experiments on MCF-7 breast cancer cells exposed to LPE WS2 show that the cells are viable and the photoluminescence of the nanosheets is detectable.

Introduction

Spurred by the intensive research on the extraordinary physical properties of graphene [1], the range of two-dimensional (2D) nanomaterials under investigation has been expanded significantly in recent years [2–8]. Prominent examples include structural analogs of graphene based on other group 14 elements (silicene [9–12], germanene [13–15], and stanene [16]), hexagonal boron nitride [17, 18], black phosphorous [19–21], and transition metal dichalcogenides (TMDCs) [22–25]. TMDCs are a large family of lamellar materials that show hexagonal symmetry in their most common polytype. Each layer consists of three superimposed homoatomic planes with an X-M-X structure, where the transition metal atoms M (typically from groups IV to VII) occupy the center of prisms formed by six chalcogens X (usually S, Se or Te). MX_2 crystals are characterized by strong covalent intralayer bonds, while weak van der Waals interactions are responsible for the interlayer stacking. The electronic, optical, chemical and mechanical properties of 2D TMDCs depend dramatically on their thickness. For instance, bulk MoS_2 shows an indirect bandgap of 1.3 eV, while single-layer nanosheets display a direct bandgap of 1.9 eV [26]. The electronic properties of single-layered TMDCs make them ideal candidates as semiconductor material in optoelectronic devices [27–36].

Ultrathin TMDCs can be obtained by synthesis, through chemical vapor deposition [22, 24, 37], or by exfoliation from the bulk. Exfoliation is carried out either in dry phase through the mechanical action of an adhesive tape or in wet phase via dispersion in a liquid, with or without the help of a chemical reaction. Although mechanical exfoliation produces large area and nearly defect-free TMDCs flakes, the process lacks scalability [38, 39]. Chemical exfoliation is usually based on the lithium intercalation (LI) method, which was developed in the 70 s [40–42] and consists of two steps: intercalation of the Li atoms and reaction of the intercalated Li with water, to produce exfoliation. To intercalate the Li, the bulk TMDC is reacted with *n*-butyllithium (BuLi) [43], typically for long reaction times and/or at high temperature; alternatively, Li can

be intercalated electrochemically or with the help of ultrasounds [44, 45]. While LI results in large quantities of single-layer TMDCs, due to the harsh reaction conditions, the TMDCs nanosheets obtained undergo a phase transition from trigonal prismatic (2H) to octahedral (1T), which is accompanied by a change in electronic properties from semiconducting to metallic [46, 47]. Although metallic 1T-MoS_2 has proven useful as electrode for the construction of supercapacitors [48], the semiconducting character of 2H TMDCs is usually of more interest, especially in applications exploiting the intrinsic band gap of TMDCs such as optoelectronics or fluorescence microscopy. The photoluminescence (PL) of MoS_2 and WS_2 is centered at around 660 nm, in the optical window of biological tissues, which opens up the possibility of bioimaging applications [49]. Therefore, the production of suspensions of luminescent TMDCs (2H polytype) is of great interest. Indeed, a method for LI exfoliation followed by 1T to 2H phase reversal has been recently reported [50].

Liquid-phase exfoliation (LPE) techniques are one of the most versatile processes to obtain few-layer 2D nanosheets [51]. The best known LPE method to obtain few layer TMDCs is the direct ultrasonication of bulk TMDC powder in adequate solvents, pioneered by Coleman and co-workers [52, 53], and later investigated by several other groups [54, 55]. Shear exfoliation methods have also been investigated, in particular for large-scale production [56]. Aqueous suspensions can also be obtained with the help of surfactants [57, 58]. LPE of layered materials generally results in a large polydispersity in thickness and lateral size, and unusual phase transitions have also been observed [59]. Therefore, it is very challenging to preserve the unique properties of single-layer nanosheets, reported for mechanically exfoliated TMDCs, in dispersions prepared by LPE. In particular, the strong PL routinely observed in mechanically exfoliated MoS_2 [60] has, to the best of our knowledge, only been described for LI exfoliated MoS_2 after deposition and annealing at 300 °C [61], and for suspensions of LPE MoS_2 after purification of the single-layers through iterative centrifugation and redispersion cycles that severely increase the preparation time and thus the production cost of the nanosheets fabricated by this method [62].

Here, we present a mild exfoliation method to produce MoS_2 and WS_2 suspensions with an outstanding density of ultrathin luminescent layers in a single step, without the need for post-treatment or purification. The method works well both in *N*-methylpyrrolidone (NMP) and in isopropanol (IPA)/water mixtures, and diluted suspensions of the luminescent nanosheets can be obtained in pure water as well as, remarkably, in cell culture medium. Incubation experiments with breast cancer MCF-7 cells demonstrate the biocompatibility of the nanosheets and their potential use in biological applications.

Results and discussion

Optimization of TMDC liquid phase exfoliation—spectroscopy and microscopy characterizations

MoS_2 LPE in NMP

The ultimate objective of this work was to develop a purification-free method to prepare suspensions of luminescent TMDC nanosheets. As a first step towards that goal, we optimized LPE exfoliation of MoS_2 in NMP in terms of MoS_2 dispersion initial concentration. We used UV–vis extinction measurements and transmission electron microscopy (TEM) imaging to characterize the optical properties (figure S1) and estimate the concentration of the final suspensions (figure S2), and analyze the size distribution of the corresponding nanoparticles (figures S3 and S4). Based on the results obtained, an initial MoS_2 concentration of $C_0 = 1$ mg ml^{-1} was found to afford the best compromise between the concentration (high enough, ~3 μg ml^{-1}) and the dimensions (low thickness, ~850 × 470 nm^2 as the lateral size) of the colloidal material. So this C_0 concentration was used to further investigate the effect of sonication time on the PL spectra of the suspensions. Figure 1(A) shows the PL spectra of MoS_2 samples sonicated for different times between 5 and 240 min. To get a fair comparison of the relative amount of luminescent nanosheets, all samples were diluted to matching extinction at the wavelength of excitation (425 nm). Samples sonicated for longer times than 30 min display two emission bands at 655 nm and 605 nm that can be ascribed to A and B excitons respectively (the latter PL arising only from bi- to few-layer MoS_2 species, which is a first indication on the composition of the corresponding colloids) [62–64]. As the sonication time increases beyond 60 min, the PL intensity decreases, while no change is observed in the position of the bands, which points to a decrease in the relative concentration of the luminescent species, rather than to a reduction in their lateral size [62]. Note that further PL characterization of colloidal suspensions prepared by sonication of $C_0 = 0.5$, 2.0 and 5.0 mg ml^{-1} MoS_2 initial dispersions showed almost no PL as compared to the above described samples, thus confirming our initial choice (figure S5).

To gather more information on the source of the PL signal, we carried out PL excitation (PLE) measurements, and compared them with the extinction spectrum (figure 1(B)). For $\lambda_{em} = 655$ nm, the PLE spectrum shows two bands, the most intense of which is located at 400–450 nm (C exciton). The second band is slightly weaker and broader, and it is found at 500–600 nm, corresponding to the B exciton. The relative intensity of the PLE maxima is consistent with the PL signal originating at least partially from few-layered MoS_2, besides single-layered nanosheets [64]. It is also interesting to note that the PLE position of all three excitons is significantly blue-shifted with respect to the extinction spectrum, where they appear at 464,

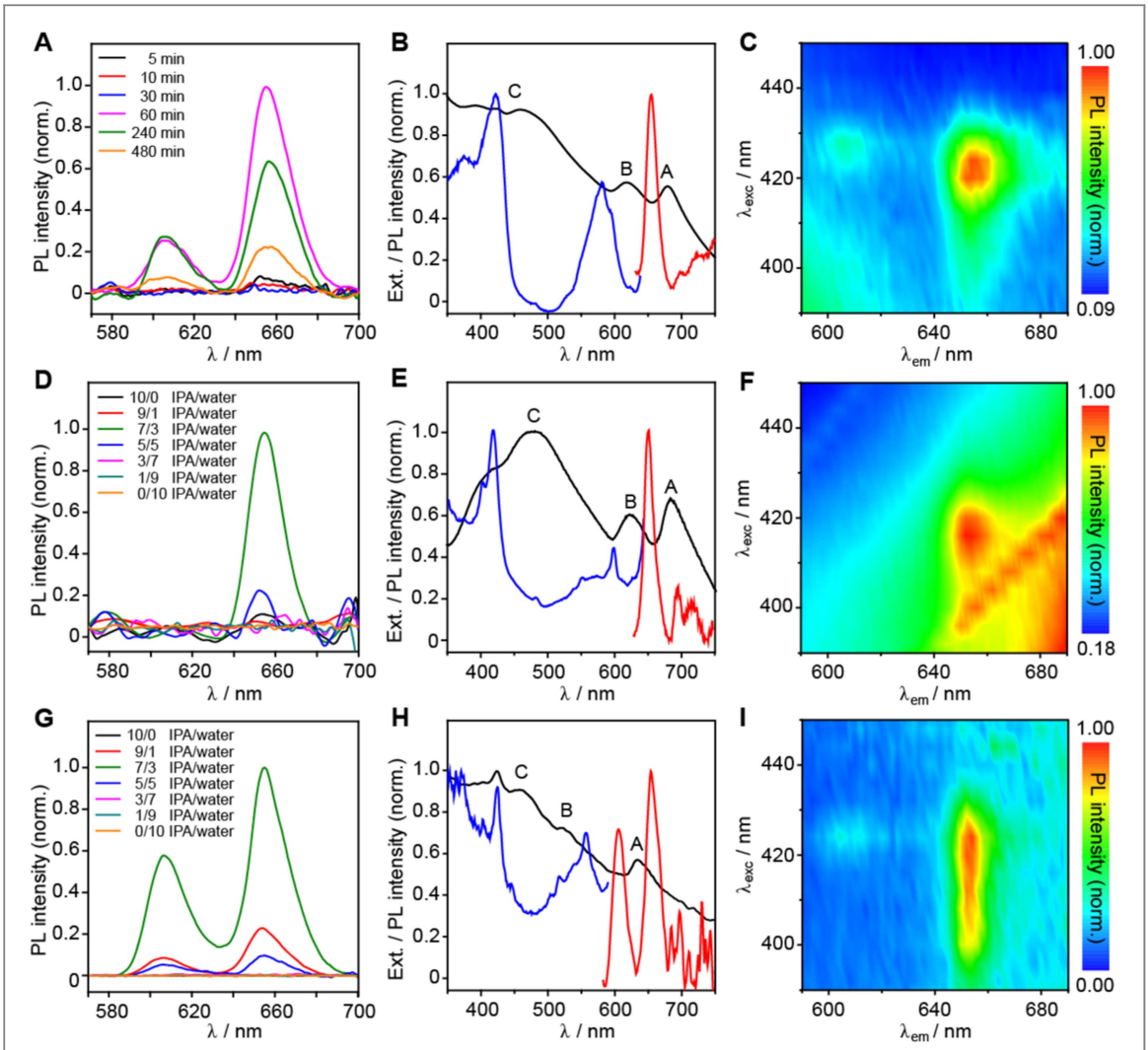

Figure 1. MoS_2 LPE in NMP: (A) PL spectra ($\lambda_{exc} = 425$ nm) of suspensions obtained after different ultrasonication times ($C_0 = 1$ mg ml^{-1}); (B) extinction (black), PLE (blue, $\lambda_{em} = 655$ nm), PL (red) spectra and (C) PLE intensity map of the sample sonicated for 60 min. MoS_2 LPE in IPA/water: (D) PL spectra ($\lambda_{exc} = 425$ nm) of suspensions obtained after 60 min ultrasonication in IPA/water mixtures ($C_0 = 1$ mg ml^{-1}); (E) extinction (black), PLE (blue, $\lambda_{em} = 655$ nm), PL (red) spectra and (F) PLE intensity map of the sample sonicated for 60 min in IPA/water 7/3. WS_2 LPE in IPA/water: (G) PL spectra ($\lambda_{exc} = 425$ nm) of suspensions obtained after 60 min ultrasonication in IPA/water mixtures ($C_0 = 1$ mg ml^{-1}); (H) extinction (black), PLE (blue, $\lambda_{em} = 610$ nm), PL (red) spectra and (I) PLE intensity map of the sample sonicated for 60 min in IPA/water 7/3. Excitons are marked with capital letters. PL spectra are baseline-corrected.

617 and 678 nm, respectively. This observation can be interpreted on the basis of the results reported by Coleman and co-workers: they observed such shifts in the extinction spectra of different MoS_2 suspensions to be especially larger as the average dimensions (number of layers and lateral size) of the nanosheets in the sample increase [62]. As a consequence, our spectroscopic results indicate that our sample is a mixture of nanosheets of different thicknesses and sizes in a particular distribution. The population of largest and thickest flakes is substantial enough regarding the population of mono-to-few-layer nanosheets to dominate the extinction, which explains the ~20 nm blue-shifts of the PLE bands as compared to the absorption bands. However, as only monolayers (and, to a far lesser extent, bi- and few-layers) [63] exhibit PL, we can deduce from the appreciable fluorescence signal detected that the relative concentration in smallest and thinnest flakes is significantly high.

Nevertheless, as the PL quantum yield (QY) of MoS_2 monolayers remains very weak and the samples exhibit large scattering, artefacts could be mistaken for a PL signal. We thus performed a PLE intensity map as a complementary measurement (figure 1(C)), which confirmed undoubtedly the PL nature of the previously observed band, with a signal centered at 655 nm, i.e. the direct bandgap emission wavelength of MoS_2 monolayers.

MoS_2 LPE in IPA/water

The use of pyrrolidone-based solvents presents many drawbacks related to their toxicity and high boiling points. Now, LPE of layered materials in mixtures of solvents with low-boiling points has already been

demonstrated to be an effective strategy for high yield exfoliation of graphite and TMDCs [54, 65, 66]. Hence, the exfoliation of MoS_2 was carried out in different mixtures of IPA and water, based on the conditions optimized in NMP: ultrasonication for 60 min at $C_0 = 1$ mg ml^{-1}.

The mild exfoliation process also produces fluorescent samples without purification in this case. However, significant PL is obtained from the IPA/water 7/3 mixture only (v/v, figure 1(D)), which is also the composition that leads to the highest concentration in colloidal material (figure S6). Indeed, such a mixture has been reported by Ajayan *et al* to maximize MoS_2 dispersion [55]. Figure 1(E) shows the corresponding PL, PLE and extinction spectra. In analogy with the suspensions in NMP, the maximum PL is obtained for 60 min sonication. The blue-shift of the excitons' bands in the PLE spectrum with respect to the extinction data is again observed in this case, due to the differences in the absorption and emission properties between thin/small nanosheets and thicker/larger ones, as already explained in detail above (see figure S7 for the distribution in lateral dimensions obtained from TEM imaging). As in the previous case, the excitation-emission contour map shown in figure 1(F) allows for the unambiguous attribution of the fluorescence signal to the PL of MoS_2 monolayers. However, the PL intensity here is weak enough to observe artefacts whose positions change according the excitation wavelength (streaks), and most probably caused by the non-negligible light scattering observed in the extinction spectrum (figures 1(D) and S6(a)).

WS_2 LPE in IPA/water

Our mild LPE conditions produce WS_2 nanosheet suspensions in IPA/water mixtures as well (figure S8). As in the case of MoS_2, luminescent colloids can be obtained without the need for purification; but quite the opposite, significant PL can be detected in a wider range of IPA volume ratio, from 50% to 90% (figure 1(G)). Nevertheless, the IPA/water 7/3 mixture remains the optimal solvent to get suspensions that are enriched in luminescent colloidal material.

The PL spectra of the above-mentioned mixtures exhibit two emission bands at 610 and 655 nm. The former can be easily attributed to the A exciton of monolayered WS_2 [64, 67, 68], whereas the latter needs to be considered more carefully. As opposed to the MoS_2 case, this second emission appears at a higher wavelength than that of A exciton, hence it cannot be assigned to B exciton PL (observed at a far lower wavelength of ~516 nm in WS_2); and as for the indirect bandgap emission from bi- and few layers, it occurs at wavelengths higher than 700 nm [67]. Otherwise, previous studies on WS_2 exfoliated either mechanically [67] or in liquid phase [68] showed a red-shifted A exciton PL due to bi- to five-layer nanosheets. Nevertheless, we discarded this possibility too, since the corresponding emissions do not exceed ~630 nm; additionally, as the PL QY decreases rapidly with the number of layers (by a factor $\sim 10^2$ for bilayers to $\sim 10^3$ for five layers) [67], such an assumption would not match with the PL relative intensities of the bands at 610 and 655 nm. Slight PL shifts, due to sample/solvent interactions in LPE and as compared to most of literature data on mechanically exfoliated samples, neither would account for our observation. Actually, the higher-wavelength PL would be in better agreement with a significantly red-shifted and intense A exciton-type emission coming from defects and/or edges, a phenomenon already observed at ~650 nm both with monolayer and few-layer nanosheets prepared by LPE [69] or CVD [62, 70]. This would be due to the tendency of excitons in WS_2 to concentrate (hence the intense PL) in the above-mentioned lattice regions; the strong exciton localization would result in a higher exciton binding energy, leading in turn to a lower-energy PL emission [70]. Other spectroscopic features of WS_2 (extinction spectrum, PLE spectrum recorded at the emission wavelength of monolayers; figure 1(H)), further examined with the sample obtained from the IPA/water 7/3 mixture, are analogous to those previously described with the MoS_2 sample, leading to a similar interpretation (see figure S9 for details on the particle size distributions).

As a further characterization of the second PL band at 655 nm, a PLE spectrum of the sample was also measured at $\lambda_{em} = 655$ nm. In that case, an intense (~10 times the PLE intensity recorded at 610 nm) and broad (FWHM ~90 nm) signal centered at 590 nm is observed (figure S10). This last result seems to confirm the edge/defect emission hypothesis. On one hand, it does not match with the characteristic PLE expected for bilayer (and few-layer) WS_2 [64], which should be quite similar to that of the monolayer (exhibiting B and C exciton absorptions). On the other hand, it reveals that the 655 nm emission is related to high absorption over a large range of wavelengths, including the A exciton wavelength. This would be consistent with excitons originating from the whole structure of mono- to multilayers (several A exciton populations differing in their binding energies), then moving to be trapped in the local potential wells of edges or defects. There they would acquire a stronger binding energy, and consequently relax by emitting a lower-energy photon.

Finally, figure 1(I) confirms the most intense fluorescence signal is the one we attribute to the defects of the nanostructure. Additionally, it evidences the emission originating purely from WS_2 monolayers is appreciable only when exciting at 425 nm.

Atomic force microscopy (AFM)

To complement the information provided by the spectroscopic data, we performed AFM measurements. Figure 2(A) shows a typical large area AFM image of a dropcast from an IPA/water 7/3 MoS_2

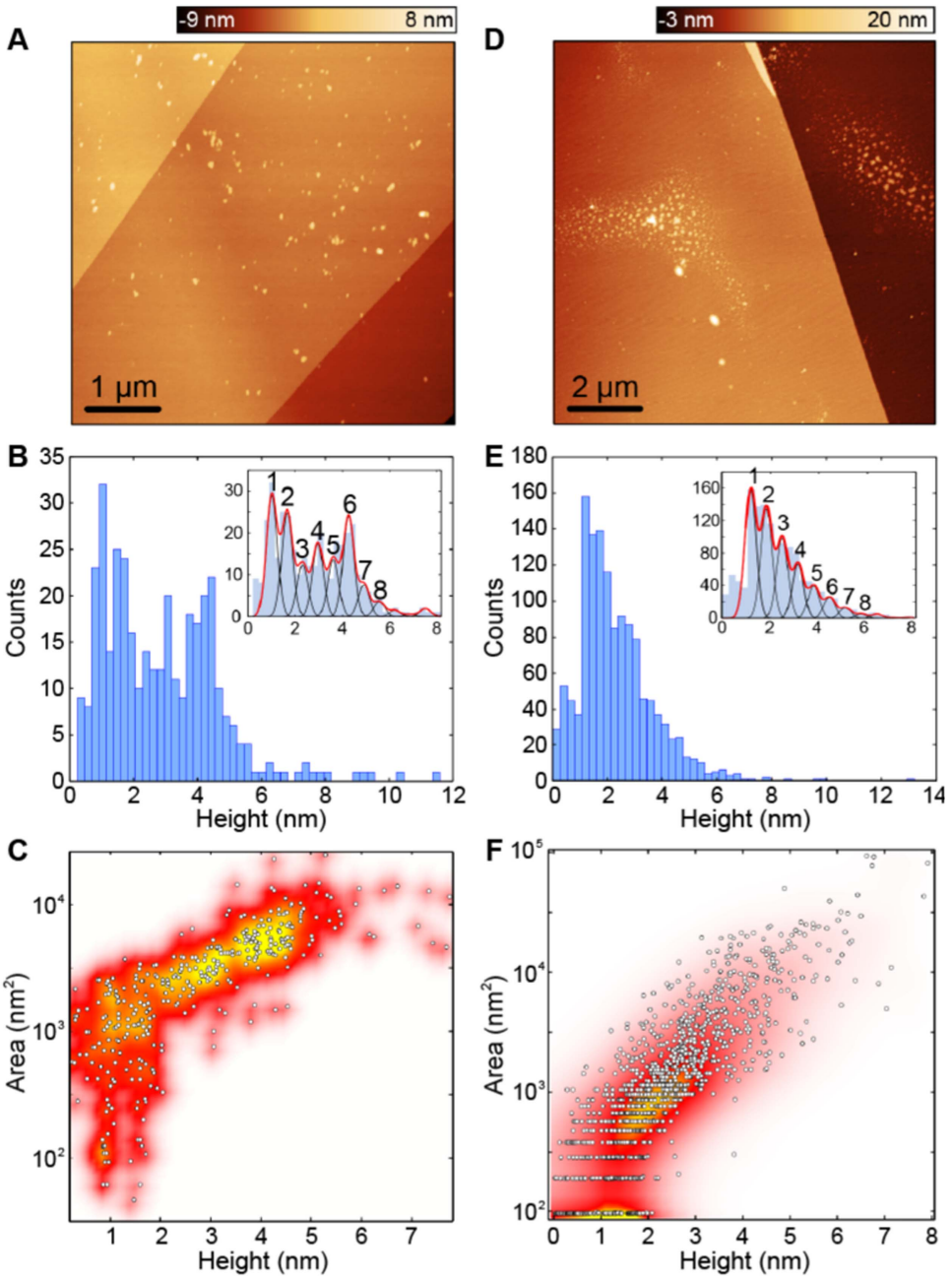

Figure 2. (A) AFM micrograph of a dropcast of a MoS_2 dispersion obtained by 60 min ultrasonication in IPA/water 7/3 ($C_0 = 1$ mg ml^{-1}). (B) Statistical analysis of the raw height data over 358 flakes and (inset) fit to the estimated number of layers (height offset = 0.4 nm). (C) Area versus height correlation of the flakes analyzed. (D) AFM micrograph of a dropcast of a WS_2 dispersion obtained by 60 min ultrasonication in IPA/water 7/3 ($C_0 = 1$ mg ml^{-1}). (E) Statistical analysis of the raw height data over 1325 flakes and (inset) fit to the estimated number of layers (height offset = 0.5 nm). (F) Area versus height correlation of the flakes analyzed. Note that the apparent horizontal lines are due to pixel size.

suspension onto a freshly cleaved mica substrate (see figure S11 for a zoomed-in micrograph). Mica has been selected for its atomically flat surface, in order to facilitate the thickness determination without artefacts arising from the substrate corrugation. Statistical analysis over 358 nanosheets is shown in figures 2(B) and (C). Raw height data show that ultrathin nanosheets are an overwhelming majority (figure 2(B)). Our data show that more than 60% of the flakes are thinner than 3 nm (~4–5 layers), and are expected to show PL. More remarkably, our analysis shows that 25% of the flakes have a thickness of 1 nm or less, a thickness value that is compatible with single-layer MoS_2. The inset in figure 2(B) shows a fit of the height histogram to multiple Gaussian curves spaced by 0.65 nm, used to determine the population of single-, bi-, tri- and multi-layers in our MoS_2 samples. Note that the Gaussians have been offset by 0.4 nm in order to obtain the best fit, this offset accounts for the adsorbates between the flake and substrate that yield to an artificially higher thickness in single layer MoS_2 prepared by liquid phase exfoliation. In fact, even

though the thickness of a pristine single-layer of MoS_2 should be ~0.65 nm, the measured height might vary with adsorbed solvent, etc and reported height values of single-layer LPE MoS_2 can be as high as 1.9 nm in the literature [62]. The area versus height data in figure 2(C) again shows that the vast majority of flakes show heights <3 nm. However, a significant cluster of large flakes of area ca. 10^4 nm^2 and of height between 4 and 5 nm also appears, and accounts for the extinction data.

Panels D–F of figure 2 show the same analyses for the WS_2 sample prepared in the same conditions. In this case, the size distribution is even narrower. In fact, more than 55% of the flakes are thinner than 2 nm, which would correspond to flakes only 1–3 layers in thickness, which is in very good agreement with the intense PL observed. The inset in figure 2(E) shows the fit of the height histogram for WS_2 samples to multiple Gaussian curves spaced by 0.65 nm to determine the population of single-, bi-, tri- and multi-layers. Here a height offset of 0.5 nm has been used to optimize the fit and account for the adsorbates between the flake and substrate.

Transmission electron microscopy

Low magnification TEM reveals the presence of ultrathin nanosheets for both MoS_2 (in NMP: figures S3 and S4; in IPA/water 7/3: figure S7) and WS_2 (figure S9). The high resolution transmission electron microscopy (HRTEM) characterization provides a more detailed study of the nanosheets, revealing areas of different degree of crystallinity and orientation. A typical situation is shown in figure 3(A) where flat crystalline 2H-polytype areas (marked as i), as confirmed by the corresponding FFT, coexist with more disordered domains, even of amorphous nature, as seen in the edge (marked as ii). The periodicity measurement in the flat hexagonal areas (0.31×0.31 nm^2) is in agreement with the 2H unit cell along the [001] zone axis. In addition, a Moiré pattern is observed in the upper part of the figure. This can be explained on the basis of the stacking of hexagonal layers mutually rotated along the *c* direction. This can be better understood in the corresponding FFT, which shows two sets of spots in hexagonal arrangements rotated by 27°. The presence of small fragments exhibiting fringe-like features have also been observed as depicted in figure 3(B). It should be noticed that the measured periodicity of 0.63 nm fits well with the interlayer MoS_2 separation. Moreover, figure 3(C) shows a HRTEM image of the WS_2 sample that clearly evidences the 2H stacking. Notice that there are only 4–5 layers, confirming the low thickness of the nanosheets.

These spectroscopic and microscopy data thus point out that the straightforward process we have developed is effective in yielding monolayer-enriched TMDC colloids. Although it appears similar to other LPE procedures, to the best of our knowledge, the only

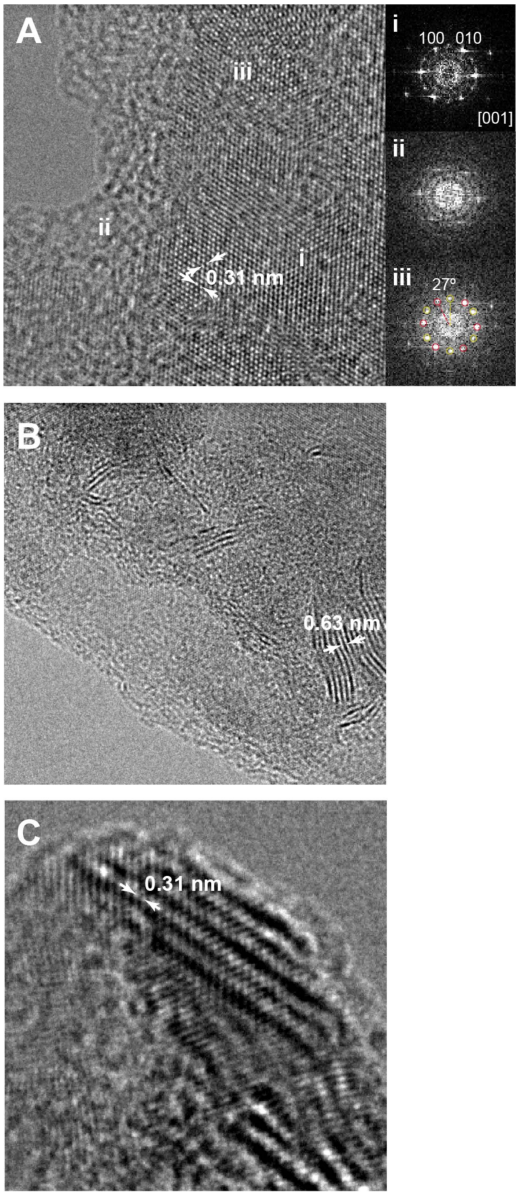

Figure 3. HRTEM characterization of (A) and (B) MoS_2 and (C) WS_2 nanosheets (magnified image) prepared from 60 min sonication of the corresponding powder dispersions in IPA/water 7/3 (C_0 = 1 mg ml^{-1}). Areas of different crystallinity and orientation are seen (insets i, ii and iii) along [001] zone axis. Figures (B) and (C) show nanosheets with layers parallel to the direction of observation.

LPE processes that have been reported to lead to fluorescent TMDC samples [62, 68, 71] required purification procedures. The key differences in our experimental procedure are: (1) the absence of additives, (2) the low initial concentration, (3) the controlled temperature during LPE, (4) the use of NMP or IPA/water mixtures as solvents. In comparison, the LPE methods reported by Coleman *et al* [62, 68] are based on probe-tip sonication, during which the actual sonication efficiency is far higher than during bath sonication, even at the same operating power [72]. Additionally, they operate in aqueous solutions of surfactants and the suspensions obtained are subjected to either higher-speed or successive

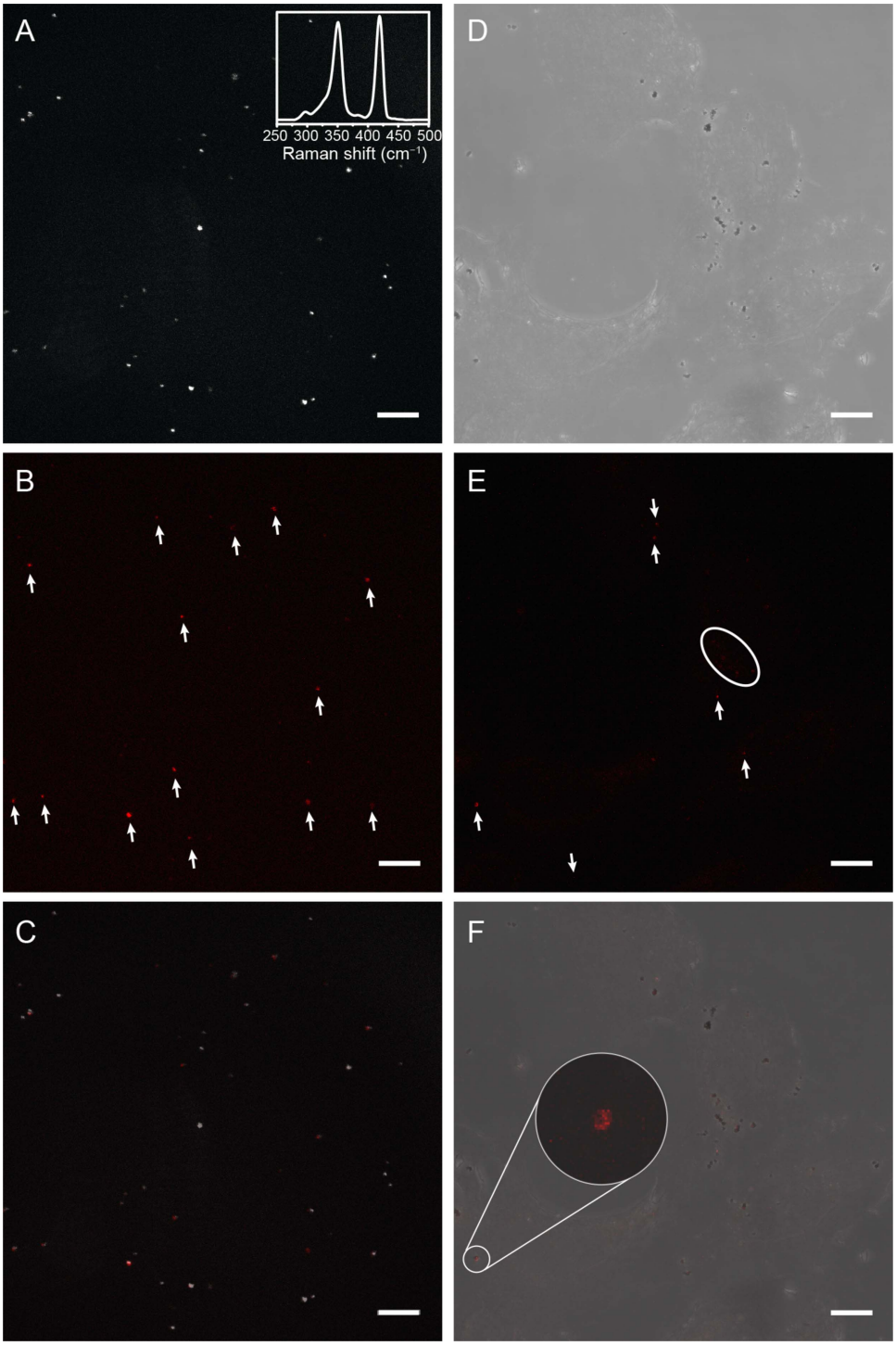

Figure 4. Confocal laser scanning microscopy images. (A) Reflexion (inset shows the Raman spectrum of the nanosheets), (B) fluorescence ($\lambda_{exc} = 405$ nm, $\lambda_{em} = 570$–700 nm; some of the photoluminescent nanosheets are marked with white arrows) and (C) overlaid confocal images of a deposition of a WS_2 dispersion ($C = 5$ μg ml^{-1}) incubated in cell culture medium at 37 °C for 4 h in the absence of cells. (D) Transmission, (E) fluorescence ($\lambda_{exc} = 405$ nm, $\lambda_{em} = 570$–700 nm; some of the photoluminescent nanosheets are marked with white arrows) and (F) overlaid confocal images of the localization of WS_2 nanosheets in human breast cancer MCF-7 cells after exposure to a WS_2 dispersion ($C = 5$ μg ml^{-1}) at 37 °C for 4 h. The inset in (F) shows a 5× zoom of the white-circled fluorescence image. Scale bars are 10 μm.

centrifugation steps, each of them lasting at least 2 h. As for the mild bath sonication conditions, they proved to lead efficiently to monolayered nanosheets (hence, exhibiting fluorescence in the case of MoS_2) from other previously reported LPE procedures [71, 73]; in those cases however, and as above, the exfoliation was performed with the help of additional binding molecules.

Experiments in biological media

Finally, considering the growing interest in the application of low-dimensional TMDCs to the biomedical

sciences [74, 75], we explored the transfer of the WS_2 luminescent nanosheets produced in IPA/water to pure water and cell culture medium. The flakes are observable either in reflection (figure 4(A)) or in transmission mode under a confocal microscope, and were unambiguously identified as WS_2 nanosheets through Raman spectroscopy, which showed the characteristic E^1_{2g} and A_{1g} Raman modes at 351 cm^{-1} and 419 cm^{-1}, respectively, in agreement with ultrathin nanosheets (inset figure 4(A)) [70]. Although the final concentration of the nanosheets in water and cell culture medium is too low for the PL to be detected in suspension, we could observe that the nanosheets showed red PL (λ_{em} = 570–700 nm) when explored under a confocal fluorescence microscope (λ_{exc} = 405 nm), as seen in figures 4(B) and (C).

When MCF-7 cells were exposed to dispersions of WS_2 nanosheets at a concentration of 5 $\mu g\,ml^{-1}$ for 4 h, PL from the exfoliated nanomaterials was weaker, but still distinctly detected, as seen by confocal fluorescence microscopy (figures 4(E) and (F); details can be found in the section F of the supporting information). The decrease in the PL of the nanomaterial is attributable to the incubation of the nanosheets within the cell microenvironment, which seems to cause the formation of aggregates. This aggregration can be easily explained by the absence of specific functionalization of the particles that would ensure their dispersion in such a complex medium. Moreover, viability studies showed no cytotoxicity of the WS_2 nanosheets at concentrations up to 10 $\mu g\,ml^{-1}$ in MCF-7 breast cancer cells (figures S12 and S13).

Conclusion

In conclusion, we have shown that it is possible to produce suspensions of MoS_2 and WS_2 sufficiently enriched in ultrathin nanosheets to observe their PL in a single LPE step, without the need for a time-consuming purification. As a proof-of-principle application, we have transferred the luminescent nanosheets to water and cell culture medium and incubated them with human breast cancer cells. The cells remain viable and the PL of WS_2 can be observed with confocal fluorescence microscopy, which paves the way for their use in biological applications. The reach of our results, however, expands to any other application where ultrathin semiconducting TMDC nanosheets are required.

Materials and methods

Colloidal nanosheet preparation

General

MoS_2 powder (<2 μm, 99%) and WS_2 powder (<2 μm, 99%) were purchased from Sigma Aldrich. Solvents were purchased from Scharlau chemicals and used as received; water was obtained from a Milli-Q filtration station ('Type 1' ultrapure water; resistivity: 18.2 MΩ cm at 25 °C). Sonications were performed in a Fisherbrand FB15051 bath sonicator (ultrasound frequency 37 kHz, 280 W, ultrasonic peak max. 320 W, standard sine-wave modulation). Samples were centrifuged using an Allegra® X-15R Beckman Colter centrifuge (FX6100 rotor).

Optimization of MoS_2 LPE in NMP

MoS_2 powder was dispersed in NMP at different initial concentrations: 0.5, 1.0, 2.0 and 5.0 $mg\,ml^{-1}$. The solutions were sonicated for various periods of time from 5 to 480 min To exclude the effect of temperature and avoid changes in the composition of the solvent due to partial evaporation or decomposition due to an increase in the temperature of the water bath during sonication, a cooling system was connected to the bath sonicator to perform the experiments at 20 °C. Aliquots of the suspensions were centrifuged at 3000 rpm (990 g) for 30 min at 25 °C. The supernatant was carefully collected.

Optimization of MoS_2 and WS_2 LPE in IPA/water mixtures

MoS_2 and WS_2 nanosheet suspensions were prepared via LPE technique by dispersing 1 $mg\,ml^{-1}$ of MoS_2 or WS_2 powder in different volume ratios of IPA/water (0/10, 1/9, 3/7, 5/5, 7/3, 9/1, 10/0). The solutions were sonicated for 60 min. As described previously, the experiments were thermostated at 20 °C. Aliquots of the suspensions were centrifuged at 3000 rpm (990 g, 25 °C) for 30 min. The supernatants containing suspended MoS_2 and WS_2 respectively were carefully collected.

WS_2 nanosheets for biocompatibility and bioimaging

WS_2 nanosheet colloidal suspensions were prepared by LPE in a 7/3 v/v mixture of IPA and water, following preceding procedure. The supernatant collected after centrifugation was evaporated under vacuum to remove isopropanol and redispersed in Milli-Q water at different concentrations.

Colloidal nanosheet characterization

Determination of nanosheet concentration

Nanosheet concentration was determined by weighing the solid residue obtained after filtration of the different colloidal suspensions. Suspensions in NMP (100 ml) were filtered through a PTFE membrane (0.1 μm nominal pore size) and dried at 150 °C overnight, whereas suspensions in IPA/water were filtered through a PVDF membrane (0.1 μm nominal pore size) and dried at 100 °C overnight.

UV–Visible spectroscopy

The extinction spectra were measured in a quartz cuvette (path length = 1 cm) with a Cary 50 UV–

visible spectrophotometer. Three independent samples were analyzed for each dispersion type.

Fluorescence spectroscopy

Photoluminescence excitation (PLE) intensity maps, PL and PLE spectra were performed on a Fluorolog®-3 HORIBA spectrofluorometer. All PL spectra were recorded at an excitation wavelength $\lambda_{exc} = 425$ nm. The samples were diluted so that their extinction at the emission wavelength does not exceed 0.1, in order to avoid possible re-absorption phenomena. The spectrum shown for each TMD dispersion is the average of the measurements carried out at least on three different and independent samples. Details on the different measurement parameters can be found in the dedicated section D of the supporting information.

Atomic force microscopy

Samples were prepared by depositing a drop (10 μl) of the suspensions on freshly cleaved mica substrates and dried under vacuum. The images were acquired using a JPK NanoWizard II AFM working in dynamic mode. NT-MDT NSG01 silicon cantilevers, with typical values of 5.1 N m^{-1} spring constant and 150 kHz resonant frequency, were employed under ambient conditions in air.

Transmission electron microscopy

Samples were prepared by drop casting of the dispersions onto a holey carbon mesh grid. Low resolution TEM observations were performed using a JEOL-JEM 2100 microscope (LaB_6 electron gun) operated at 200 kV. HRTEM images were obtained with a JEOL-JEM 2100F instrument (field-effect electron gun, 2.5 Å resolution).

Acknowledgments

We gratefully acknowledge funding from the European Research Council (MINT, ERC-StG-307609), from the EU (EC FP7-PEOPLE-2013-CIG (no. 631396), from the MINECO of Spain (CTQ2014-60541-P RYC-2014-01406, RYC RYC-2012-11231 and MAT2014-58399-JIN), and from the Comunidad Autónoma de Madrid (MAD2D P2013/MIT-3007).

References

[1] Geim A K and Novoselov K S 2007 The rise of graphene *Nat. Mater.* **6** 183–91
[2] Miro P, Audiffred M and Heine T 2014 An atlas of two-dimensional materials *Chem. Soc. Rev.* **43** 6537–54
[3] Xu M, Liang T, Shi M and Chen H 2013 Graphene-like two-dimensional materials *Chem. Rev.* **113** 3766–98
[4] Tang Q and Zhou Z 2013 Graphene-analogous low-dimensional materials *Prog. Mater. Sci.* **58** 1244–315
[5] Mas-Balleste R, Gomez-Navarro C, Gomez-Herrero J and Zamora F 2011 2D materials: to graphene and beyond *Nanoscale* **3** 20–30
[6] Rao C N R, Ramakrishna Matte H S S and Maitra U 2013 Graphene analogues of inorganic layered materials *Angew. Chem., Int. Ed. Engl.* **52** 13162–85
[7] Le Lay G, Salomon E, De Padova P, Layet J-M and Angot T 2014 The rise of elemental two-dimensional materials beyond graphene *Aust. J. Chem.* **67** 1370–2
[8] Butler S Z *et al* 2013 Progress, challenges, and opportunities in two-dimensional materials beyond graphene *ACS Nano* **7** 2898–926
[9] Kara A, Enriquez H, Seitsonen A P, Lew Yan Voon L C, Vizzini S, Aufray B and Oughaddou H 2012 A review on silicene—new candidate for electronics *Surf. Sci. Rep.* **67** 1–18
[10] Vogt P, De Padova P, Quaresima C, Avila J, Frantzeskakis E, Asensio M C, Resta A, Ealet B and Le Lay G 2012 Silicene: compelling experimental evidence for graphenelike two-dimensional silicon *Phys. Rev. Lett.* **108** 155501
[11] Feng B, Ding Z, Meng S, Yao Y, He X, Cheng P, Chen L and Wu K 2012 Evidence of silicene in honeycomb structures of silicon on Ag(111) *Nano Lett.* **12** 3507–11
[12] Johnson N W, Vogt P, Resta A, De Padova P, Perez I, Muir D, Kurmaev E Z, Le Lay G and Moewes A 2014 The metallic nature of epitaxial silicene monolayers on Ag(111) *Adv. Funct. Mater.* **24** 5253–9
[13] Li L, Lu S-Z, Pan J, Qin Z, Wang Y-Q, Wang Y, Cao G-Y, Du S and Gao H-J 2014 Buckled germanene formation on Pt(111) *Adv. Mater.* **26** 4820–4
[14] Dávila M E, Xian L, Cahangirov S, Rubio A and Lay G L 2014 Germanene: a novel two-dimensional germanium allotrope akin to graphene and silicene *New J. Phys.* **16** 095002
[15] Derivaz M, Dentel D, Stephan R, Hanf M-C, Mehdaoui A, Sonnet P and Pirri C 2015 Continuous germanene layer on Al(111) *Nano Lett.* **15** 2510–6
[16] Zhu F-F, Chen W-J, Xu Y, Gao C-L, Guan D-D, Liu C-H, Qian D, Zhang S-C and Jia J-F 2015 Epitaxial growth of two-dimensional stanene *Nat. Mater.* **14** 1020–5
[17] Pakdel A, Bando Y and Golberg D 2014 Nano boron nitride flatland *Chem. Soc. Rev.* **43** 934–59
[18] Golberg D, Bando Y, Huang Y, Terao T, Mitome M, Tang C and Zhi C 2010 Boron nitride nanotubes and nanosheets *ACS Nano* **4** 2979–93
[19] Liu H, Neal A T, Zhu Z, Luo Z, Xu X, Tomanek D and Ye P D 2014 Phosphorene: an unexplored 2D semiconductor with a high hole mobility *ACS Nano* **8** 4033–41
[20] Buscema M, Groenendijk D J, Blanter S I, Steele G A, van der Zant H S J and Castellanos-Gomez A 2014 Fast and broadband photoresponse of few-layer black phosphorus field-effect transistors *Nano Lett.* **14** 3347–52
[21] Li L, Yu Y, Ye G J, Ge Q, Ou X, Wu H, Feng D, Chen X H and Zhang Y 2014 Black phosphorus field-effect transistors *Nat. Nanotechnol.* **9** 372–7
[22] Lv R, Terrones H, Elías A L, Perea-López N, Gutiérrez H R, Cruz-Silva E, Rajukumar L P, Dresselhaus M S and Terrones M 2015 Two-dimensional transition metal dichalcogenides: clusters, ribbons, sheets and more *Nano Today* **10** 559–92
[23] Chhowalla M, Liu Z and Zhang H 2015 Two-dimensional transition metal dichalcogenide (TMD) nanosheets *Chem. Soc. Rev.* **44** 2584–6
[24] Lv R, Robinson J A, Schaak R E, Sun D, Sun Y, Mallouk T E and Terrones M 2015 Transition metal dichalcogenides and beyond: synthesis, properties, and applications of single- and few-layer nanosheets *Acc. Chem. Res.* **48** 56–64
[25] Wang Q H, Kalantar-Zadeh K, Kis A, Coleman J N and Strano M S 2012 Electronics and optoelectronics of two-dimensional transition metal dichalcogenides *Nat. Nanotechnol.* **7** 699–712
[26] Zeng H and Cui X 2015 An optical spectroscopic study on two-dimensional group-VI transition metal dichalcogenides *Chem. Soc. Rev.* **44** 2629–42
[27] Jariwala D, Sangwan V K, Lauhon L J, Marks T J and Hersam M C 2014 Emerging device applications for semiconducting two-dimensional transition metal dichalcogenides *ACS Nano* **8** 1102–20

[28] Kang K, Xie S, Huang L, Han Y, Huang P Y, Mak K F, Kim C-J, Muller D and Park J 2015 High-mobility three-atom-thick semiconducting films with wafer-scale homogeneity *Nature* **520** 656–60

[29] Chen M, Nam H, Rokni H, Wi S, Yoon J S, Chen P, Kurabayashi K, Lu W and Liang X 2015 Nanoimprint-assisted shear exfoliation (NASE) for producing multilayer MoS_2 structures as field-effect transistor channel arrays *ACS Nano* **9** 8773–85

[30] Cui Y *et al* 2015 High-performance monolayer WS_2 field-effect transistors on high-$\varkappa$dielectrics *Adv. Mater.* **27** 5230–4

[31] Ma Y, Liu B, Zhang A, Chen L, Fathi M, Shen C, Abbas A N, Ge M, Mecklenburg M and Zhou C 2015 Reversible semiconducting-to-metallic phase transition in chemical vapor deposition grown monolayer WSe_2 and applications for devices *ACS Nano* **9** 7383–91

[32] Mayorga-Martinez C C, Ambrosi A, Eng A Y S, Sofer Z and Pumera M 2015 Metallic 1T-WS_2 for selective impedimetric vapor sensing *Adv. Funct. Mater.* **25** 5611–6

[33] Furchi M M, Polyushkin D K, Pospischil A and Mueller T 2014 Mechanisms of photoconductivity in atomically thin MoS_2 *Nano Lett.* **14** 6165–70

[34] Baugher B W H, Churchill H O H, Yang Y and Jarillo-Herrero P 2014 Optoelectronic devices based on electrically tunable p–n diodes in a monolayer dichalcogenide *Nat. Nanotechnol.* **9** 262–7

[35] Ross J S *et al* 2014 Electrically tunable excitonic light-emitting diodes based on monolayer WSe_2 p–n junctions *Nat. Nanotechnol.* **9** 268–72

[36] Radisavljevic B, Radenovic A, Brivio J, Giacometti V and Kis A 2011 Single-layer MoS_2 transistors *Nat. Nanotechnol.* **6** 147–50

[37] Shi Y, Li H and Li L-J 2015 Recent advances in controlled synthesis of two-dimensional transition metal dichalcogenides via vapour deposition techniques *Chem. Soc. Rev.* **44** 2744–56

[38] Li H, Wu J, Yin Z and Zhang H 2014 Preparation and applications of mechanically exfoliated single-layer and multilayer MoS_2 and WSe_2 nanosheets *Acc. Chem. Res.* **47** 1067–75

[39] Novoselov K S, Jiang D, Schedin F, Booth T J, Khotkevich V V, Morozov S V and Geim A K 2005 Two-dimensional atomic crystals *Proc. Natl Acad. Sci. USA* **102** 10451–3

[40] Dines M B 1975 Lithium intercalation via butyllithium of the layered transition metal dichalcogenides *Mater. Res. Bull.* **10** 287–91

[41] Murphy D W, Di Salvo F J, Hull G W Jr and Waszczak J V 1976 Convenient preparation and physical properties of lithium intercalation compounds of Group 4B and 5B layered transition metal dichalcogenides *Inorg. Chem.* **15** 17–21

[42] Whittingham M S and Gamble F R Jr 1975 Lithium intercalates of the transition metal dichalcogenides *Mater. Res. Bull.* **10** 363–71

[43] Joensen P, Frindt R F and Morrison S R 1986 Single-layer MoS_2 *Mater. Res. Bull.* **21** 457–61

[44] Wang L, Xu Z, Wang W and Bai X 2014 Atomic mechanism of dynamic electrochemical lithiation processes of MoS_2 nanosheets *J. Am. Chem. Soc.* **136** 6693–7

[45] Yuwen L, Yu H, Yang X, Zhou J, Zhang Q, Zhang Y, Luo Z, Su S and Wang L 2016 Rapid preparation of single-layer transition metal dichalcogenide nanosheets via ultrasonication enhanced lithium intercalation *Chem. Commun.* **52** 529–32

[46] Ambrosi A, Sofer Z and Pumera M 2015 Lithium intercalation compound dramatically influences the electrochemical properties of exfoliated MoS_2 *Small* **11** 605–12

[47] Wang Y *et al* 2013 Electrochemical control of photoluminescence in two-dimensional MoS_2 nanoflakes *ACS Nano* **7** 10083–93

[48] Acerce M, Voiry D and Chhowalla M 2015 Metallic 1T phase MoS_2 nanosheets as supercapacitor electrode materials *Nat. Nanotechnol.* **10** 313–8

[49] Weissleder R 2001 A clearer vision for *in vivo* imaging *Nat. Biotechnol.* **19** 316–7

[50] Fan X, Xu P, Zhou D, Sun Y, Li Y C, Nguyen M A T, Terrones M and Mallouk T E 2015 Fast and efficient preparation of exfoliated 2H MoS_2 nanosheets by sonication-assisted lithium intercalation and infrared laser-induced 1T to 2H phase reversion *Nano Lett.* **15** 5956–60

[51] Nicolosi V, Chhowalla M, Kanatzidis M G, Strano M S and Coleman J N 2013 Liquid exfoliation of layered materials *Science* **340** 1226419

[52] Coleman J N *et al* 2011 Two-dimensional nanosheets produced by liquid exfoliation of layered materials *Science* **331** 568–71

[53] Cunningham G, Lotya M, Cucinotta C S, Sanvito S, Bergin S D, Menzel R, Shaffer M S P and Coleman J N 2012 Solvent exfoliation of transition metal dichalcogenides: dispersibility of exfoliated nanosheets varies only weakly between compounds *ACS Nano* **6** 3468–80

[54] Zhou K-G, Mao N-N, Wang H-X, Peng Y and Zhang H-L 2011 A mixed-solvent strategy for efficient exfoliation of inorganic graphene analogues *Angew. Chem., Int. Ed. Engl.* **50** 10839–42

[55] Shen J *et al* 2015 Liquid phase exfoliation of two-dimensional materials by directly probing and matching surface tension components *Nano Lett.* **15** 5449–54

[56] Varrla E, Backes C, Paton K R, Harvey A, Gholamvand Z, McCauley J and Coleman J N 2015 Large-scale production of size-controlled MoS_2 nanosheets by shear exfoliation *Chem. Mater.* **27** 1129–39

[57] Smith R J *et al* 2011 Large-scale exfoliation of inorganic layered compounds in aqueous surfactant solutions *Adv. Mater.* **23** 3944–8

[58] Guardia L, Paredes J I, Rozada R, Villar-Rodil S, Martinez-Alonso A and Tascon J M D 2014 Production of aqueous dispersions of inorganic graphene analogues by exfoliation and stabilization with non-ionic surfactants *RSC Adv.* **4** 14115–27

[59] Shmeliov A, Shannon M, Wang P, Kim J S, Okunishi E, Nellist P D, Dolui K, Sanvito S and Nicolosi V 2014 Unusual stacking variations in liquid-phase exfoliated transition metal dichalcogenides *ACS Nano* **8** 3690–9

[60] Splendiani A, Sun L, Zhang Y, Li T, Kim J, Chim C-Y, Galli G and Wang F 2010 Emerging photoluminescence in monolayer MoS_2 *Nano Lett.* **10** 1271–5

[61] Eda G, Yamaguchi H, Voiry D, Fujita T, Chen M and Chhowalla M 2011 Photoluminescence from chemically exfoliated MoS_2 *Nano Lett.* **11** 5111–6

[62] Backes C *et al* 2014 Edge and confinement effects allow *in situ* measurement of size and thickness of liquid-exfoliated nanosheets *Nat. Commun.* **5** 4576

[63] Zhao W, Ribeiro R M and Eda G 2015 Electronic structure and optical signatures of semiconducting transition metal dichalcogenide nanosheets *Acc. Chem. Res.* **48** 91–9

[64] Kozawa D *et al* 2014 Photocarrier relaxation pathway in two-dimensional semiconducting transition metal dichalcogenides *Nat. Commun.* **5** 4543

[65] Halim U, Zheng C R, Chen Y, Lin Z, Jiang S, Cheng R, Huang Y and Duan X 2013 A rational design of cosolvent exfoliation of layered materials by directly probing liquid–solid interaction *Nat. Commun.* **4** 2213

[66] Zhou K-G, Zhao M, Chang M-J, Wang Q, Wu X-Z, Song Y and Zhang H-L 2015 Size-dependent nonlinear optical properties of atomically thin transition metal dichalcogenide nanosheets *Small* **11** 694–701

[67] Zhao W, Ghorannevis Z, Chu L, Toh M, Kloc C, Tan P-H and Eda G 2013 Evolution of electronic structure in atomically thin sheets of WS_2 and WSe_2 *ACS Nano* **7** 791–7

[68] Backes C *et al* 2016 Production of highly monolayer enriched dispersions of liquid-exfoliated nanosheets by liquid cascade centrifugation *ACS Nano* **10** 1589–601

[69] Chow P K, Jacobs-Gedrim R B, Gao J, Lu T-M, Yu B, Terrones H and Koratkar N 2015 Defect-induced photoluminescence in monolayer semiconducting transition metal dichalcogenides *ACS Nano* **9** 1520–7

[70] Gutiérrez H R, Perea-López N, Elías A L, Berkdemir A, Wang B, Lv R, López-Urías F, Crespi V H, Terrones H and Terrones M 2013 Extraordinary room-temperature photoluminescence in triangular WS_2 monolayers *Nano Lett.* **13** 3447−54
[71] Guan G *et al* 2015 Protein induces layer-by-layer exfoliation of transition metal dichalcogenides *J. Am. Chem. Soc.* **137** 6152–5
[72] Dhanalakshmi N P and Nagarajan R 2011 Ultrasonic intensification of the chemical degradation of methyl violet: an experimental study *Int. J. Chem. Mol. Nucl. Mater. Metall. Eng.* **59** 1019–24
[73] Bernal M M and Pérez E M 2015 One-pot exfoliation of graphite and synthesis of nanographene/dimesitylporphyrin hybrids *Int. J. Mol. Sci.* **16** 10704–14
[74] Xu S, Li D and Wu P 2015 One-pot, facile, and versatile synthesis of monolayer MoS_2/WS_2 quantum dots as bioimaging probes and efficient electrocatalysts for hydrogen evolution reaction *Adv. Funct. Mater.* **25** 1127–36
[75] Cheng L, Yuan C, Shen S, Yi X, Gong H, Yang K and Liu Z 2015 Bottom-up synthesis of metal-ion-doped WS_2 nanoflakes for cancer theranostics *ACS Nano* **9** 11090–101